Turbulent diapycnal mixing in the subtropical northwestern Pacific: Spatial-seasonal variations and role of eddies

Zhao Jing,[1] Lixin Wu,[1] Lei Li,[1] Chengyan Liu,[1] Xi Liang,[1] Zhaohui Chen,[1] Dunxin Hu,[2] and Qingyu Liu[1]

Received 16 March 2011; revised 21 July 2011; accepted 25 July 2011; published 19 October 2011.

[1] Both spatial and seasonal variation of turbulent diapycnal mixing in the subtropical northwestern Pacific are evaluated by employing a fine-scale parameterization method based on profiles of potential density, which are obtained from CTD measurements during our recent hydrographic surveys implemented by the China National Key Basic Research Project from 2008 to 2010 and the World Ocean Circulation Experiment. Over smooth seafloor, the value of diffusivity away from the boundary is comparable with the values observed in the stratified midlatitude ocean interior, i.e., O (10^{-5} m^2 s^{-1}). On the other hand, enhanced diapycnal mixing, i.e., O (10^{-4} m^2 s^{-1}) or larger has been found over rough topography such as the Central Basin Trough, Okidaito Ridge, the origin of the Kuroshio Current, and especially Luzon Strait, which might result from dissipation of baroclinic energy generated when barotropic tides rub over rough topography. Over flat bathymetry, mixing is probably stirred by the wind work on near inertial motions in the upper 600 m and enhanced downward propagating energy has been found in the presence of anticyclonic eddies, which points to the important role of anticyclonic eddies in enhancing the diapycnal mixing at greater depth. The diffusivity also displays a distinct seasonal variation with strong (weak) mixing corresponding to strong (weak) wind-input energy in winter (summer), which, however, is only confined to upper 600 m. This is different from the midlatitude northwestern Pacific, where seasonality of diffusivity can be found at 1500-m depth.

Citation: Jing, Z., L. Wu, L. Li, C. Liu, X. Liang, Z. Chen, D. Hu, and Q. Liu (2011), Turbulent diapycnal mixing in the subtropical northwestern Pacific: Spatial-seasonal variations and role of eddies, *J. Geophys. Res.*, *116*, C10028, doi:10.1029/2011JC007142.

1. Introduction

[2] Turbulent diapycnal mixing in the ocean controls the transport of heat, modifies water masses, and maintains ocean stratification. Understanding the spatial and temporal variation of diapycnal diffusivity is important for improving the representation and prediction of large-scale ocean circulation and climate with numerical models [*Saenko and Merryfield*, 2005; *Wunsch and Ferrari*, 2004]. With the traditional one-dimensional advection–diffusion model, *Munk* [1966] argued that an average vertical diffusivity K of O (10^{-4} m^2 s^{-1}) is required to maintain the observed abyssal stratification. However, the last three decades of microstructure measurements have indicated a much smaller diapycnal diffusivity value, i.e., O (10^{-5} m^2 s^{-1}), in the stratified midlatitude ocean interior away from boundaries [*Gregg*, 1987; *Polzin et al.*, 1997; *Kunze et al.*, 2006]. Several possible mechanisms have been proposed to resolve this discrepancy, varying from enhanced mixing over rough topography to wind-driven diapycnal fluxes in the Southern Ocean [*Toggweiler and Samuels*, 1998]. In the past 20 years, elevated diapycnal diffusivities, i.e., O (10^{-4} m^2 s^{-1}) or larger have been found to occur over rough bathymetry such as ridges [*Althaus et al.*, 2003; *Klymak et al.*, 2006], seamounts [*Kunze and Toole*, 1997; *Lueck and Mudge*, 1997], canyons [*St. Laurent et al.*, 2001; *Carter and Gregg*, 2002], as well as hydraulically controlled passages [*Roemmich et al.*, 1996; *Polzin*, 1996; *Ferron et al.*, 1998].

[3] Much of the oceanic mixing away from boundaries occurs through internal wave breaking. Energy input by tides and wind primarily furnishes the internal wavefield [*Wunsch and Ferrari*, 2004]. Internal tides are generated where the barotropic tide flows over rough bathymetry. While a small fraction of the resultant energy goes into high modes that can dissipate locally, the bulk will radiate at low vertical modes [*St. Laurent et al.*, 2002; *St. Laurent and Garrett*, 2002], and it remains unknown where this part of energy dissipates. Besides, the internal lee waves can also be generated as geostrophic flows impinge on rough topography [*Polzin*, 1999; *Polzin*, 2004], which might play a very

[1] Physical Oceanography Laboratory, Ocean University of China, Qingdao, China.
[2] Key Laboratory of Ocean Circulation and Wave, Chinese Academy of Sciences, Qingdao, China.

0148-0227/11/2011JC007142

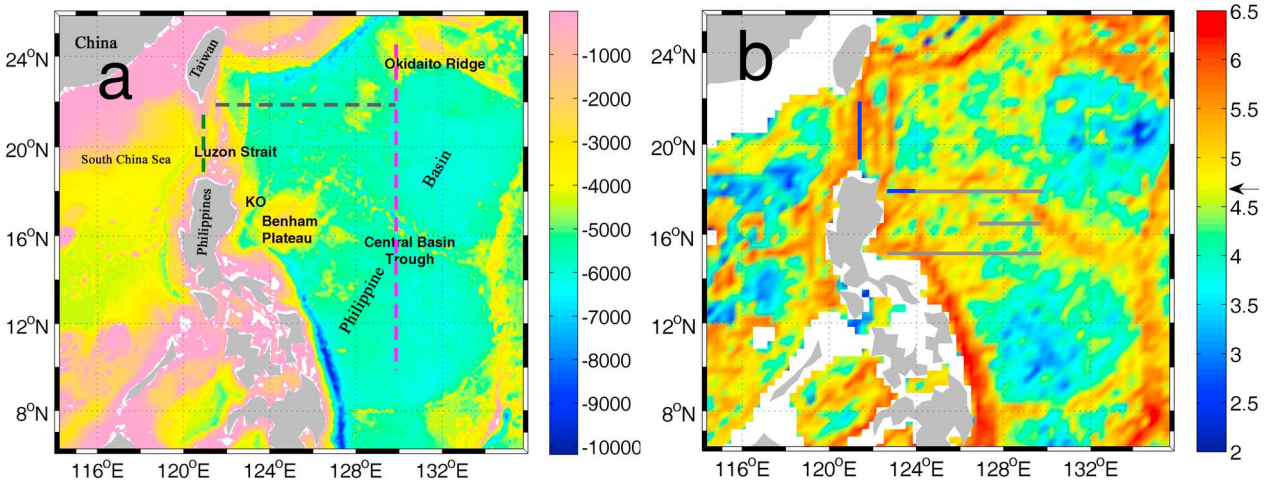

Figure 1. (a) WOCE Section P08N (pink dashed), PR20 (gray dashed), and PR21 (green dashed) along with the bathymetry in the subtropical northwestern Pacific (unit: m). The abbreviation "KO" represents the origin of the Kuroshio Current. (b) The hydrographic sections of our recent four surveys along with the map of topographic roughness: the blue solid represents the repeated sections which have been observed during each cruise, and the gray solid represents the ones only observed during Cruise 4. The color bar represents $\log_{10}$ (Roughness) in m^2, and the arrow points to the critical value distinguishing the smooth bathymetry from rough topography.

important role in maintaining the enhanced mixing founded in the Southern Ocean [*Naveira Garabato et al.*, 2003]. Though the elevated diapycnal mixing above rough bathymetry has been well demonstrated by the previous observations, it is still poorly understood how far the enhanced mixing is able to extend and this might vary from one site to another due to the different topographic roughness as well as the strength of bottom flow [*Polzin*, 2004].

[4] On the other hand, the energy flux input from the wind to near inertial motions in the upper ocean mixed layer is another main source to sustain the turbulent diapycnal mixing [*Alford*, 2003]. However, it has been argued whether a substantial part of wind-input energy can propagate downward to sustain the subsurface and deep ocean mixing [*Wunsch and Ferrari*, 2004]. By using a numerical model, *Zhai et al.* [2005] demonstrated that the leakage of near-inertial energy out of the surface layer is strongly enhanced in the presence of the eddies, with the anticyclonic eddies acting as a conduit to the deep ocean. Nevertheless, it remains uncertain to what extent the anticyclonic eddies could modulate the diapycnal mixing under surface layer and more observations are still needed.

[5] It is conceivable that seasonal and interannual variations of the wind stress and mesoscale eddies may lead to similar variations in turbulent diapycnal mixing throughout the upper ocean globally. Although the low-frequency variations of turbulent diapycnal mixing so far are still poorly understood, they are critically important for improving models' ability in evaluation and prediction of changes of large-scale ocean circulation [e.g., *Richards et al.*, 2009].

[6] The subtropical northwestern Pacific contains a full spectrum of bathymetric features and a wide range of ocean conditions. The seafloor is almost flat and featureless in the Philippine Basin with much rougher topography around Philippine Islands, Benham Plateau, Central Basin Trough, Okidaito Ridge, and especially Luzon Strait (Figure 1). Besides, the tidal dissipation here is also considerably variable with the energy dissipation at Luzon Strait orders of magnitude larger than that in the remaining places [*Egbert and Ray*, 2000; *Tian et al.*, 2009]. Therefore, the subtropical northwestern Pacific serves as a miniature of the global ocean to some extent and a thorough knowledge of diapycnal mixing here would be very useful to expand our understanding of the global mixing. In addition, recent analysis of historical hydrographic data collected to the south of Japan Island reveals that seasonality of diapycnal mixing penetrates to great depth, pointing to the important role of wind-input near inertial energy in furnishing the subsurface and deep-ocean mixing [*Jing and Wu*, 2010]. However, whether this holds throughout the world ocean remains uncertain due to the limited data sets. Therefore, it would be very helpful to analyze the seasonal variation here and make a comparison with previous study.

[7] In this paper we apply a fine-scale parameterization developed by *Kunze et al.* [2006] to CTD profiles collected here by our recent hydrographic surveys and the World Ocean Circulation Experiment (WOCE) to analyze both the spatial and seasonal variation of turbulent diapycnal mixing and the controlling mechanisms.

[8] The paper is organized as follows. Data and methodology are given in section 2. Results and analysis are presented in section 3. The validation of the estimates by a fine-scale parameterization method is tested in section 4. Finally, the paper is concluded with a summary and some discussions are included in section 5.

2. Data and Methodology

2.1. Data

[9] Since October 2008, we have so far carried out four cruises to a number of sites in the subtropical northwestern

Table 1. Start Time, End Time, and the Number of Profiles Collected in Different Regions During Each Cruise

	Cruise 1	Cruise 2	Cruise 3	Cruise 4	Total
Luzon Strait[a]	6	11	4	8	29
KO[b]	3	5	6	14	28
Smooth	0	0	0	19	19
Others[c]	0	1	1	23	25
Start time	20080917[d]	20090709	20091203	20101115	
End time	20080928	20090729	20091220	20110105	

[a]Luzon Strait is defined as region 120°E–122°E, 18°N–22°N.
[b]The abbreviation "KO" represents the origin of Kuroshio Current, which is defined as region 122°E–124°E, 18°N.
[c]"Others" means the profiles located over rough bathymetry but not located at Luzon Strait and in the origin of Kuroshio Current.
[d]The digits "20080917" means 17 September 2008.

Pacific (Figure 1b and Table 1). Data were collected using a Seabird 9–11 Plus CTD and a Seabird 9–17 Plus with sensors sampling at 24 Hz. The accuracy of conductivity and temperature are 0.0003 S m^{-1} (corresponding to an accuracy of about 0.003 psu for salinity) and 0.001°C, respectively. The CTD is lowered at a rate of 0.5 m s^{-1} and only the data collected during downcasts are used here. Temperature and conductivity values were aligned in time to correct for sensor-response-lag effects according to the Instruction Manual supplied by SeaBird Electronics, Inc. Then the data were averaged to half-second (2 Hz) values to reduce random noise, which results in an approximate 0.25-m vertical resolution. During four cruises, there were 101 profiles collected in the Luzon Strait and subtropical northwestern Pacific (Table 1). On the other hand, the CTD measurements from WOCE Section P08N, PR20, and PR21 are also employed here (Figure 1a). These profiles have 2-m vertical resolution. Uncertainties are 0.0005°C for temperature and 0.002 psu for salinity [*Kunze et al.*, 2006]. The data spanned from year 1990 to year 1996. Only the profiles located within the latitude band 0–25°N are used here, which results in 155 profiles in total (Table 2).

[10] Besides, we also use the 6-h sea surface wind stress in the same period from NCAR/NCEP Reanalysis [*Kalnay et al.*, 1996] and the merged satellite altimetry sea surface height anomaly data provided by AVISO with a 1-day temporal resolution as well as a 1.3° longitude Mercator spatial grid.

[11] Finally the ETOPO2v2 (2-Minute Gridded Global Relief Data) are used to evaluate the topographic roughness var(h) in a 1/3° × 1/3° domain square, where h represents the topographic height [*Kunze et al.*, 2006]. Here the smooth bathymetry is defined as regions with the roughness value less than 5×10^4 m^2, and the rough topography as that with value larger than 5×10^4 m^2. The critical value is chosen by visually inspecting Figures 1b and 4c, and a minor change of this value does not result in any substantial difference for the results here.

2.2. Fine-Scale Parameterization Method

[12] Based on the idea that weakly nonlinear interactions between a well-developed sea of internal waves act to steadily transport energy from the large (vertical) scales at which it is generated and propagates, to the small scales at which waves break due to shear or convective instabilities, the diapycnal diffusivity can be expressed in terms of fine-scale strain as [*Kunze et al.*, 2006]

$$\kappa = K_0 \frac{\langle \xi_z^2 \rangle^2}{{}_{GM}\langle \xi_z^2 \rangle^2} h_2(R_\omega) j(f/N) \tag{1}$$

where $K_0 = 0.5 \times 10^{-5}$ m^2 s^{-1}, ${}_{GM}\langle \xi_z^2 \rangle$ is strain variance from the Garrett-Munk model spectrum [*Gregg and Kunze*, 1991] treated in the same way as the observed strain variance $\langle \xi_z^2 \rangle$:

$$j(f/N) = \frac{f \cdot \mathrm{Arc\,cosh}(N/f)}{f_{30} \cdot \mathrm{Arc\,cosh}(N_0/f_{30})} \tag{2}$$

$$h2(R_\omega) = \frac{1}{6\sqrt{2}} \frac{R_\omega (R_\omega + 1)}{\sqrt{R_\omega - 1}} \tag{3}$$

$f_{30} = f(30°)$, $N_0 = 5.2 \times 10^{-3}$ rad s^{-1}, and R_ω represents shear/strain variance ratio, which is fixed at 7 in this paper.

[13] Internal wave strain is estimated from buoyancy frequency $\xi_z = (N^2(z) - \overline{N}^2)/\overline{N}^2$, where $N^2(z)$ is computed from the vertical difference of potential density and mean stratification, and $\overline{N}^2$ is based on quadratic fits to each profile segment [*Polzin et al.*, 1995]. Then Fourier transforming gives the spectral representation $\phi(k)$, and a spectral correction is employed to compensate the attenuation at higher wave numbers due to the difference operator used to calculate strain [*Polzin et al.*, 2002]. Strain variance $\langle \xi_z^2 \rangle$ is determined by integrating $\phi(k)$ from a minimum vertical wave number $k_{\min}$ out to a maximum wave number $k_{\max}$ [*Kunze et al.*, 2006] so that

$$\langle \xi_z^2 \rangle = \int_{k_{\min}}^{k_{\max}} \phi(k) dk \le 0.1 \tag{4}$$

The GM strain variance is computed over the same wave number band so that

$$\left\langle \xi_{z,GM}^2 \right\rangle = \frac{\pi E_0 b j_*}{2} \int_{k_{\min}}^{k_{\max}} \frac{k^2}{(k + k_*)^2} dk \tag{5}$$

where $E_0 = 6.3 \times 10^{-5}$ is the dimensionless energy level, b = 1300 m the scale depth of the thermocline, $j_* = 3$ the reference mode number and $k_* = (\pi \cdot j_* \cdot N)/(b \cdot N_0)$ the reference wave number with $N_0 = 5.2 \times 10^{-3}$ rad s^{-1} [*Gregg and Kunze*, 1991].

[14] The dissipation rate can be expressed in the form of

$$\varepsilon = K \frac{N^2}{\Gamma} \tag{6}$$

where Γ is mixing efficiency and typically taken to be 0.2 [*Osborn*, 1980]. In this paper, the vertically integrated

Table 2. The Number of WOCE Profiles Collected in Different Regions

	P08N	PR20	PR21	Total
Luzon Strait	0	21	22	43
KO	0	0	0	0
Smooth	39	40	0	79
Others	16	17	0	33

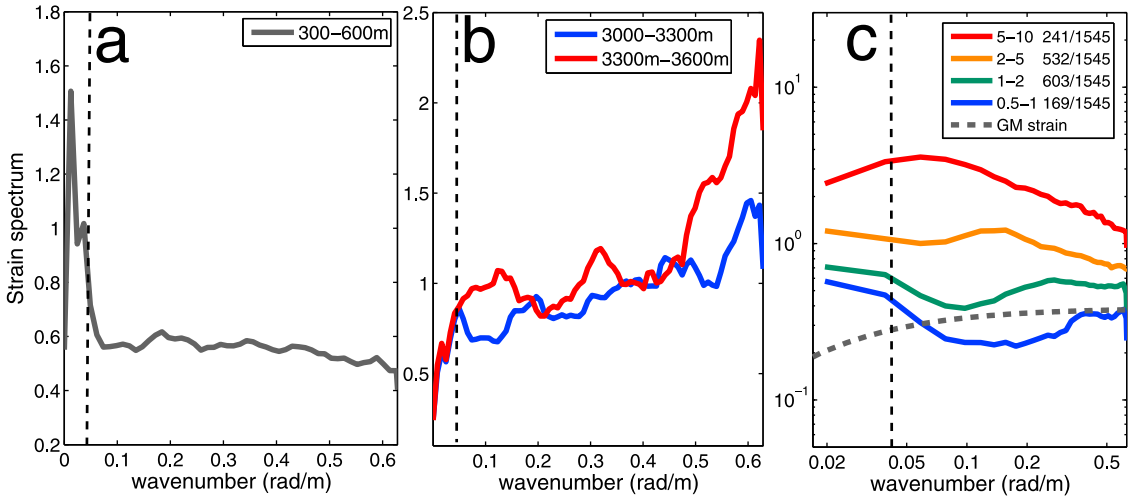

Figure 2. The averaged vertical wave number spectra for strain over smooth bathymetry (a) at the uppermost segment and (b) at the lowermost two segments. (c) The vertical wave number spectra for strain (color solid) binned with respect to the GM-normalized strain variance (legend to right) and the GM model strain spectrum (gray dashed). Vertical dashed lines denote the lower integration limit for strain variance. Note that the linear scale for both x and y axes is used in Figures 2a and 2b but the logarithmic scale is used in Figure 2c.

dissipation rate from depth D_1 to depth D_2 represents $\int_{D_1}^{D_2} \rho \cdot \varepsilon \cdot dz$, where ρ is the density of seawater.

[15] As profiles of horizontal velocity are not available, it is difficult to estimate R_ω. Based on 3500 lowered ADCP/CTD profiles from the Indian, Pacific, North Atlantic, and Southern Oceans, *Kunze et al.* [2006] found that for $N > 4.5 \times 10^{-4}$ s^{-1} the measured shear/strain variance ratio $R_\omega = 7 \pm 3$ is a little over twice the canonical GM value of 3 in diverse situations. Here, a fixed value, i.e., $R_\omega = 7$ is used, which might lead to uncertainties probably about a factor of 2 by invoking the equation (3). As the fine-scale parameterization was only able to reproduce microstructure diffusivities to within a factor of 2 [*Polzin et al.*, 1995], the total uncertainties inherent in our results would probably be within a factor of 4.

[16] Finally, all the profiles are broken into 300-m segments to evaluate the strain spectra and then the segment-averaged diffusivity. In the upper ocean the strain spectrum may be contaminated due to great depth variability in the background stratification, which means that the method is not applicable in the presence of sharp pycnoclines. Therefore, the shallowest segment, i.e., 0–300 m, is discarded by following *Kunze et al.* [2006]. At deeper segment, i.e., 300–600 m over smooth bathymetry, the excessive redness of the spectra due to strong depth changes in the background stratification is almost confined to the lowest resolved wave numbers, i.e., 0.04 rad m^{-1} (Figure 2a) and thus the contamination is negligible.

[17] The strain spectra might also be contaminated by density noise, and the contamination would be more serious in the region with weak background stratification and low strain variance. Typically, spectra of raw quantities should be red, flattening out at some high wave number where noise becomes significant. Since strain is a gradient quantity, its spectra will be flatter and noise will appear blue. Below 3000 m over smooth topography where the background stratification is extremely weak, the spectra appear blue throughout the whole wave band (Figure 2b). Therefore, the strain variance evaluated in these regions is not reliable and should be treated cautiously.

[18] Figure 2c displays vertical wave number spectra for strain in the upper 3000 m binned with respect to GM-normalized strain variance $\langle \xi_z^2 \rangle / \langle \xi_{z,GM}^2 \rangle$. These have GM-normalized strain variances ranging from 0.5 to 1 to 5–10 with about 90% of the segments having $\langle \xi_z^2 \rangle / \langle \xi_{z,GM}^2 \rangle$ larger than 1. Therefore, the strain spectral level is generally higher than that of GM model. For low variances, the strain spectra tend to be flat or slightly blue at mid-wave numbers (λ = 10–150 m) and as strain variances increase, the mid-wave number spectral level rises and becomes flatter.

[19] By employing a Lillefors test [*Lilliefors*, 1967], we find the estimated values of K and ε among all the profiles tend to be more close to a lognormal distribution compared with a normal distribution. So all the average values relevant to K and ε are computed as the geometric mean rather than the arithmetic mean in this paper.

2.3. Thorpe-Scale Method

[20] The dissipation rate for a single density overturn event is [*Thorpe*, 1977]

$$\varepsilon_i = a^2 \cdot L_T^2 \cdot N^3 \tag{7}$$

where $a = 0.8$ is a constant of proportionality [*Dillon*, 1982], N buoyancy frequency, and L_T the Thorpe scale which is a measure of the vertical length scale of density overturns that, in a stratified fluid, are associated with gravitational instabilities.

[21] Potential density is used for the overturn analysis. Here, σ_θ, σ_2 and σ_4 are used for the water column shallow than 1000 m, between 1000 m and 3000 m, and below 3000 m, respectively. For each turbulent overturn (here

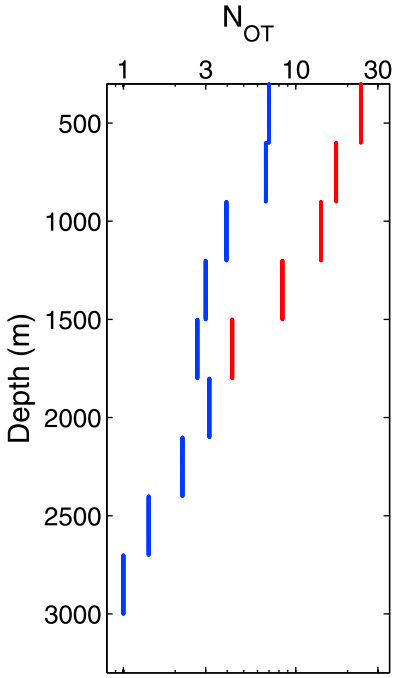

Figure 3. Averaged number of overturns per 300-m segment (N_{OT}) over smooth topography (blue solid), and at Luzon strait where the bottom is much rougher (red solid).

overturn is defined by following *Dillon* [1984]), L_T is calculated as the RMS vertical displacement required to reorder the observed potential density profile into a gravitationally stable one [*Thorpe*, 1977], and N is evaluated from the gradient of reordered profile within the vertical boundaries of each overturn to avoid overestimation [*Finnigan et al.*, 2002].

[22] The segment-mean dissipation rate is evaluated following *Finnigan et al.* [2002] in the form of

$$\varepsilon = \frac{\sum_i \varepsilon_i L_i}{D} \tag{8}$$

Here D = 300 m represents the total depth of the segment and L_i is the thickness for a single overturn. It should be noted that the Thorpe-scale method is not applicable to the WOCE data because of the limit of the vertical resolution of the data (2 m).

[23] Both spatial resolution of the measurements and noise of the instruments may impose constraints on the overturn detection [*Galbraith and Kelley*, 1996]. Because in situ noise levels may exceed manufacturer statements for a variety of reasons, here a run length criterion is used to detect inversions created by noise, and then RMS noise level was estimated from Thorpe fluctuations of these noisy inversions [*Galbraith and Kelley*, 1996]. We employ this criterion to all the overturns detected in the profiles collected during our 4 cruises. The cutoff run length is about 8 for the data analyzed in this paper. We evaluate the RMS noise level for each overturn with run length less than the cutoff value. About 90 percent of these noise-induced overturns have a RMS noise level less than 0.5×10^{-3} kg m^{-3}, which is therefore set to be the noise level in our analysis. Using the overturn size criteria of *Galbraith and Kelley* [1996] yields the minimum detectable overturn size for our data:

$$L_z = 5\Delta z = 1.25\,\mathrm{m} \tag{9}$$

$$L_\rho = \frac{2g}{N^2}\frac{\delta\rho}{\rho_0} \approx \frac{9.5 \times 10^{-6}\,\mathrm{m\,s^{-2}}}{N^2} \tag{10}$$

In this paper, overturns with size less than either L_z or L_ρ are treated as artifacts and are discarded.

[24] Besides, though temperature and conductivity values are aligned in time to correct for sensor-response-lag effects according to the Instruction Manual, it might not be able to eliminate salinity spikes or T/S mismatches exhaustively in the real ocean. Here, the R_0 criterion proposed by *Gargett and Garner* [2008] is employed to eliminate the artificial overturns produced by salinity spikes.

[25] Figure 3 shows the number of overturns that occurs in each 300-m vertical segment over smooth bathymetry and at Luzon Strait respectively. Over smooth bathymetry, the number of overturns is about 7 in the uppermost two segments and then decreases rapidly with the increasing depth. Between 900 m and 3000 m, the number gradually drops from 4 to 1 (Figure 3). A similar decrease in overturn occurrence with depth can be also observed at Luzon Strait but the number of occurrence is much larger. The average drops from about 20 in the shallowest segment to less than 5 below 1500 m (Figure 3).

3. Results and Analysis

3.1. Spatial Distribution

[26] The diapycnal diffusivity in the northwestern Pacific displays great spatial variability (Figures 4 and 5). Figures 4a and 4b show the background stratification and diffusivity along the meridional section 130°E. The background stratification strengthens slightly with the increasing latitude in the upper ocean but has nearly no meridional variation below 1000 m. On the other hand, the diffusivity does not show similar spatial distribution with background stratification. It can be seen from Figure 4b that over smooth bathymetry, the value of diffusivity away from the boundary is about O (10^{-5} m^2 s^{-1}), comparable with the values observed in the stratified midlatitude ocean interior. However, enhanced diapycnal mixing, i.e., O (10^{-4} m^2 s^{-1}) extends to around 1500 m above the seafloor in the vicinity of the Central Basin Trough and Okidaito Ridge where the bathymetry is much rougher (Figure 4c). Similar cases can also be found at the origin of the Kuroshio Current and at Luzon Strait where the seafloor is rough (Figures 5a and 5b) and elevated mixing is throughout the whole water column. To further analyze the relation of diapycnal mixing with topography, we compute the vertical wave number spectra for strain averaged among all the profiles over smooth and rough bathymetry, respectively. It can be seen from Figure 5c that the strain spectral level over rough bathymetry is about twofold of that over smooth topography between the lowest resolved wave number and 0.03 cpm, and at higher wave numbers the discrepancy becomes somewhat smaller.

[27] The much stronger mixing detected is probably due to the dissipation of baroclinic energy generated when bar-

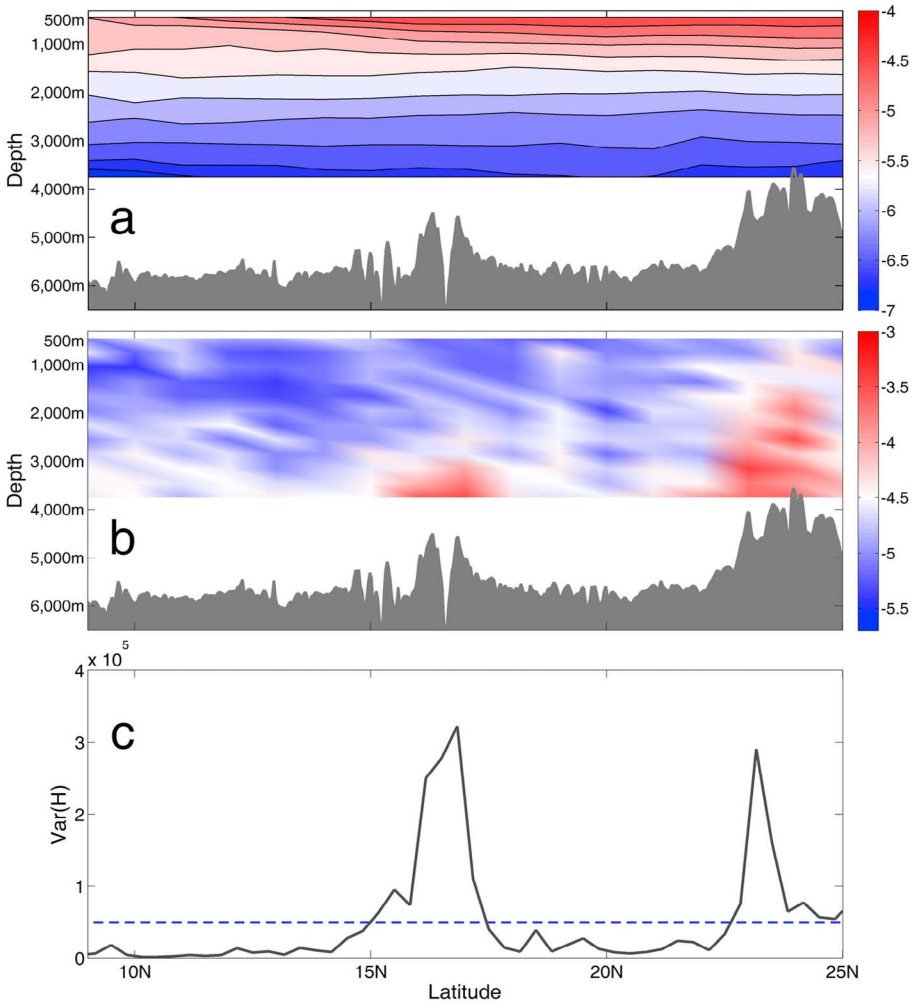

Figure 4. Spatial distribution along the meridional section 130°N: (a) for the time-mean background stratification $\log_{10}(N^2)$ in s^{-2}, (b) for the time-mean diapycnal diffusivity $\log_{10}(K)$ in $m^2\ s^{-1}$ and (c) for the bottom roughness in m^2. The blue dashed line in Figure 4c represents the cutoff between rough and smooth.

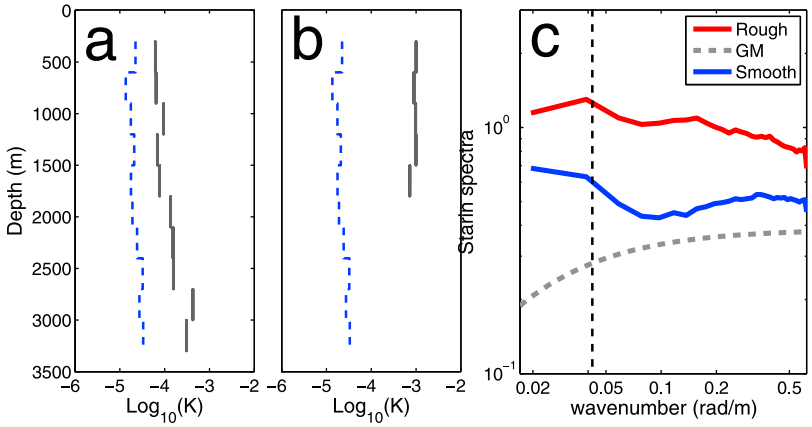

Figure 5. The averaged vertical profiles of diffusivity in $m^2\ s^{-1}$ (gray solid) (a) in the origin of Kuroshio Current and (b) at Luzon Strait. The blue dashed line represents the mean value averaged among all the profiles located over smooth bathymetry. (c) The vertical wave number spectra for strain averaged among all the profiles over smooth bathymetry (blue solid) and among all the profiles over rough bathymetry (red solid). The gray dashed line represents the GM model spectrum, and the vertical dashed line demarks the lower integration limit for strain variance.

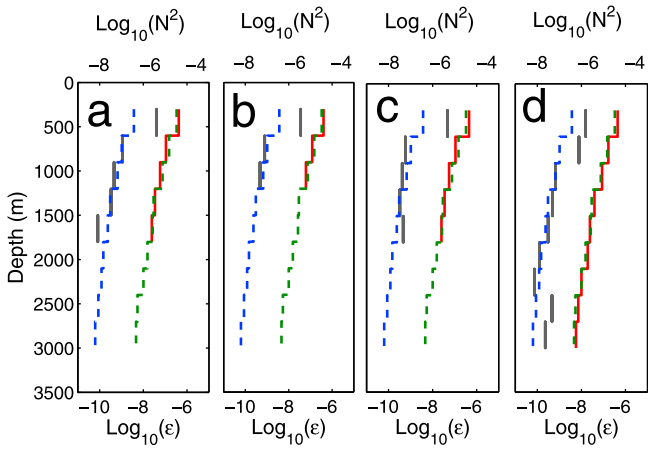

Figure 6. Four CTD profiles with enhanced dissipation rate ($m^2\ s^{-3}$, gray solid) and the corresponding background stratification (red solid) at (a) 16.5°N, 128°E, (b) 16.5°N, 130°E, (c) 16.5°N, 130°E, and (d) 18°N, 124.5°E. The first three profiles were collected on 26 November 2010; the final one was collected on 12 December 2009. The green and blue dashed lines represent the values of stratification and dissipation rate averaged among all the profiles over smooth bathymetry, respectively.

otropic tides rub over rough topography [*St. Laurent et al.*, 2002]. However, it should be noted that though the roughness values, i.e., $O\ (10^5\ m^2)$ are comparable in these regions, the value of diffusivity in Luzon Strait, i.e., $O\ (10^{-3}\ m^2\ s^{-1})$ is an order of magnitude larger than that at the origin of the Kuroshio Current, Central Basin Trough and Okidaito Ridge. This discrepancy might result from a much larger baroclinic energy flux in Luzon Strait [*Egbert and Ray*, 2000; *Tian et al.*, 2009].

3.2. Wind-Driven Mixing in the Upper Ocean and Seasonality

[28] Though the enhanced mixing over rough bathymetry here is possibly sustained by the tidal input energy, it remains uncertain what dominates the diapycnal mixing in the upper ocean over smooth topography. Away from the direct influence of boundary processes, most of the ocean mixing is driven by breaking internal gravity waves, with the wind work on near inertial motions being one of the major energy sources for the internal wavefield in the upper ocean [*Wunsch and Ferrari*, 2004]. Figure 6 shows the background stratification, i.e., $\overline{N}^2$, and dissipation rate ε averaged among all the 98 profiles over smooth topography. The most striking feature is the depletion of ε below 600 m. The dissipation rate in the uppermost segment is $3.7 \times 10^{-9}\ m^2\ s^{-3}$, about four times of that in the following one, i.e., $1.0 \times 10^{-9}\ m^2\ s^{-3}$. As the discrepancy of $\overline{N}^2$ between these two segments is only about a factor of 2, such depletion cannot simply result from the stronger background stratification in the uppermost segment. Instead, it probably implies an energy source located at the sea surface. Therefore, it is conceivable to expect that the wind-input energy plays an important role in furnishing the diapycnal mixing in the upper ocean, especially for the segment 300–600 m. To assess our conjecture, an energy budget is calculated as the first step.

[29] The energy flux from the wind to near inertial motions can be directly estimated using observed surface wind stress and mixed layer velocity data. However, only the former is usually available from observations. Here we use a simple slab model introduced by *Pollard and Millard* [1970], which allows us to compute the energy flux by only using wind stress data. The equations for the velocity components, u and v of a mixed layer are [*D'Asaro*, 1985]

$$\frac{dZ}{dt} + (r + i \cdot f)Z = \frac{T}{H} \tag{11}$$

where $Z = u + i \cdot v$ is the mixed layer current, f is Coriolis parameter, H is the mixed-layer depth, $T = (\tau_x + i \cdot \tau_y)/\rho$ is the wind stress, and r is the frequency-dependent damping parameter [*Alford*, 2003]

$$r = r_o\left(1 - e^{-\sigma^2/2\sigma_c^2}\right) \tag{12}$$

where σ represents the angular frequency, $r_o = 0.15\ f$ and $\sigma_c = f/2$.

[30] Fourier transformation of the equation (11) gives a spectral solution:

$$\hat{Z}(\sigma) = \frac{\hat{T}(\sigma)}{H}\frac{r - i(f + \sigma)}{r^2 + (f + \sigma)^2} \tag{13}$$

Then $Z(t)$ can be obtained by Fourier transforming $\hat{Z}(\sigma)$ back and the near-inertial energy flux is calculated as [*Alford*, 2003]

$$\Pi = \mathrm{Re}\left(\rho \cdot Z \cdot T^*\right) \tag{14}$$

Finally, the wind work is daily averaged to match the in situ observations.

[31] The errors inherent in the slab model to calculate wind-input near inertial energy result from many aspects. The wind work might be underestimated by up to a factor of 2 owing to the finite temporal and spatial resolution of the NCEP winds, or overestimated by approximately the same factor owing to inadequacies in the slab model [*Alford and Whitmont*, 2007]. Despite these uncertainties, the estimated order of magnitude of the wind work is reliable and the model would be suitable for our qualitative analysis here.

[32] The vertically integrated dissipation rates averaged among all the 98 profiles over the smooth bathymetry within 300–600 m and 300–2100 m are about $1.2 \times 10^{-3}\ W\ s^{-2}$ and $2.0 \times 10^{-3}\ W\ s^{-2}$, respectively, comparable to the time-mean wind work on near inertial motions approximately in the same region, i.e., $2.4 \times 10^{-3}\ W\ s^{-2}$. This implies that the wind-input energy has an important role in maintaining diapycnal mixing in the upper ocean from the view of energy balance.

[33] The wind work on near inertial motions usually varies among different seasons resulting from the annual cycle of the sea surface wind stress. Therefore, there might be seasonal variations inherent in diapycnal mixing, if the mixing is powered by wind-input energy. On the other hand, the seasonality of diapycnal mixing might also serve as convincing evidence for the wind-maintained mixing, because the mixing mainly furnished by tidal dissipation is unlikely to have any seasonal variation. Therefore, to further

Table 3. Distribution by Latitude and Season of the Profiles Within the Box 8°N–22°N, 126°E–130°E

Latitude	FMA	MJJ	ASO	NDJ
8°–12°	0	11	0	4
12°–17°	0	17	0	15
17°–22°	0	24	9	9

verify the wind-maintained mixing in the upper ocean, we analyze the seasonality of diffusivity.

[34] To calculate the seasonal variation, only the profiles located in the narrow box, i.e., (8°N–22°N, 126°E–130°E) are used to ensure that the profiles in different seasons are approximately located at the same longitudes. (A detailed depiction about spatial distribution of these profiles is listed in Table 3.) All the profiles in this box are located over smooth bathymetry except those over the Central Basin Trough. However, as shown in our paper, the enhanced mixing due the interaction of bottom flow with rough topography is only confined to water column below 3000-m depth. Therefore, it is reasonable to include the profiles over the Central Basin Trough to analyze the seasonality in the upper ocean, which results in 52 profiles in summer and 28 in winter. Here, winter is defined as November, December and January, and summer is defined as May, June and July. Such an unconventional definition of the seasons is due to our data coverage because more than 80% of the profiles over smooth bathymetry were collected during these six months.

[35] It can be seen from Figure 7b that in the shallowest segment the mean value of diffusivity in winter is more than twofold of that in summer, which corresponds to much larger wind-input energy in winter, i.e., 3.3×10^{-3} W m^{-2} than that in summer, i.e., $1.2. \times 10^{-3}$ W m^{-2} (Figure 7a). What's more, in consideration of the dependence of diffusivity on latitude resulting from

$$j(f/N) = \frac{f \cdot \mathrm{Arc\,cosh}(N/f)}{f_{30} \cdot \mathrm{Arc\,cosh}(N_0/f_{30})},$$

it is necessary to make sure that the seasonality is not an artifact due to the latitude. Here, we calculate the average latitude for the profiles collected in each season and the mean latitude in summer, i.e., 16.2°N is similar with that in winter, i.e., 15.3°N (Table 3). Furthermore, we also evaluate the diffusivity in winter and summer by removing the factor $j(f/N)$. It can be seen from Figures 7b and 7c that the seasonal variation is pronounced in both cases. Therefore, a distinct seasonality in segment 300–600 m is reliable, which further verifies the critical role of wind-input near inertial energy in maintaining diapycnal mixing in the upper ocean. On the other hand, there is no evident seasonality in the deeper segment 600–900 m (Figure 8a), suggesting that the most of wind-input energy may dissipate in the upper 300–600 m and is not able to further propagate downward to supply energy for mixing in deeper region, consistent with the rapid attenuation of dissipation rate below 600 m.

[36] To make a comparison, we also evaluate the seasonality at Luzon Strait and the origin of the Kuroshio Current where the bathymetry is much rougher. Not surprisingly, there is no distinct seasonality in the upper ocean (Figures 8b and 8c), because the diapycnal mixing in the whole water column over these regions is probably maintained by the tidal dissipation which has no seasonal variations.

3.3. Role of Anticyclonic Eddies in Draining Energy to Great Depth

[37] While the mean dissipation rate in the shallowest segment over smooth bathymetry is only about 3.7×10^{-9} m^2 s^{-3}, four profiles display much larger values exceeding 10^{-8} m^2 s^{-3} (Figure 6). The first three profiles (Figures 6a, 6b, and 6c) were collected on 26 November 2010, located at 16.5°N, 128°E and 16.5°N, 130°E. The vertically integrated dissipation rate from 300 m to 600 m averaged among these three profiles is about 11.2×10^{-3} W m^{-2}, almost an order of magnitude larger than the mean value. As the diapycnal mixing in the upper ocean over smooth bathymetry is mainly furnished by wind work on near inertial motions and the enhanced mixing only confined to the uppermost segment also implies an energy source located at the surface, it is conceivable that the elevated mixing may result from the burst of wind-input energy. Because rays of near inertial waves propagate horizontally when propagating downward, the horizontal location of the energy-input region might not

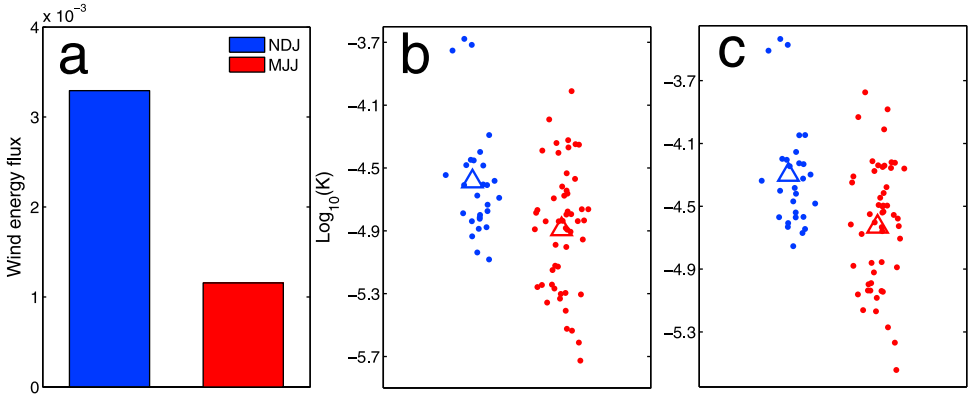

Figure 7. Different physical variables in winter (November, December, and January) and in summer (May, June, July) in the box (8°N–22°N, 126°E–130°E): (a) wind work on near inertial motions; (b) scatterplot of diffusivity in segment 300–600 m with the factor $j(f/N)$ retained and (c) that with the factor removed. The triangle represents the mean value.

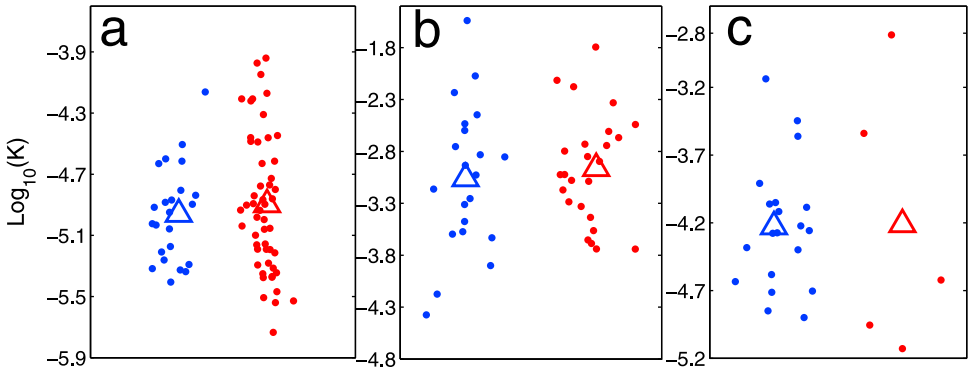

Figure 8. Scatterplot of diapycnal diffusivity at (a) segment 600–900 m in the box (8°N–22°N, 126°E–130°E), (b) segment 300–600 m at Luzon Strait, and (c) segment 300–600 m in the origin of Kuroshio Current for winter (blue dots) and summer (red dots). The triangle represents the mean value. All values here are evaluated with the factor $j(f/N)$ retained.

necessarily be in accord with the place where the profiles were collected. On the other hand, rays of near inertial waves typically reach the bottom within 400 km of their source [*Garrett*, 2001] except within 10° of the equator and poles (where we have no data). Therefore, only the wind work in the vicinity needs to be inspected here.

[38] Figure 9a displays the wind work on near inertial motions at sites 16.2°N, 127.5°E, 20°N, 127.5°E, 16.2°N, 131.3°E and 20°N, 131.3°E. There are only three energy-burst events with energy flux compatible with the enhanced vertically integrated dissipation rate, i.e., O (10×10^{-3} W m^{-2}). One is just around the day when these three profiles were collected, the others about 40 and 30 days earlier, i.e., 16 October 2010 and 27 October 2010. Due to the limited data, it is impossible to calculate the time which it takes for the wind-input energy to propagate from the surface where it is generated to great depth where it is dissipated. So it is difficult to decide which one accounts for the enhanced mixing. However, as the time needed ranges typically from a few days to several weeks due to various ocean conditions [*Alford and Gregg*, 2001; *Garrett*, 2001], the elevated mixing is more likely to result from the energy burst on 16 October 2010 or 27 October 2010.

[39] On the other hand, enhanced mixing is also found in the fourth profile collected on 12 December 2009 located at 18°N, 124.5°E (Figure 6d). The vertically integrated dissipation rate from 300 m to 900 m is about $7.2. \times 10^{-3}$ W m^{-2}, which might be furnished by the burst of wind energy in the surrounding region about a dozen or so days before (Figure 9b). However, unlike the previous profiles, the elevated dissipation rate extends down to 900-m depth, which means enhanced downward-propagating near inertial energy. There must be some additional mechanisms accounting for such an enhancement.

[40] As *Kunze* [1985] argued, in the presence of geostrophic background flow, the geostrophic vorticity ζ shifts

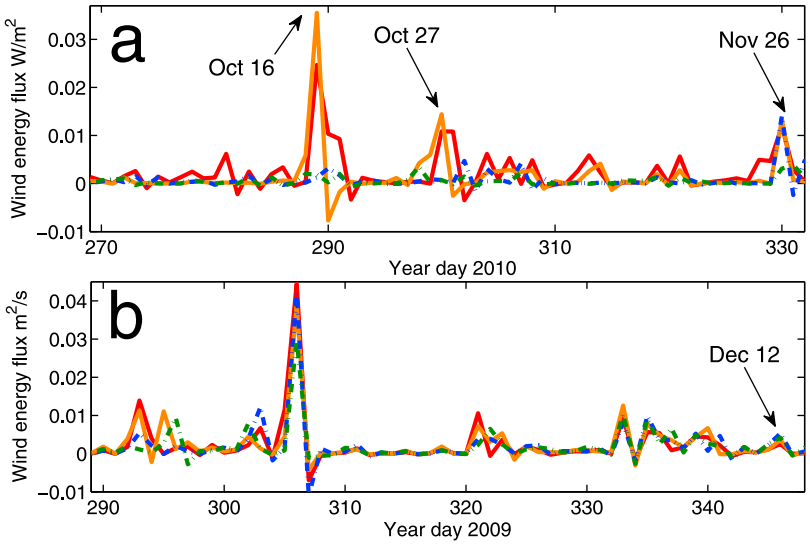

Figure 9. Time series of wind work on near inertial motions at different sites: (a) 16.2°N, 127.5°E (blue dashed), 20°N, 127.5°E (red solid), 16.2°N, 131.3°E (green dashed) and20°N, 131.3°E (orange solid); (b) 18.1°N, 123.8°E (blue dashed), 20°N, 123.8°E (red solid), 18.1°N, 125.6°E (green dashed) and 20°N, 125.6°E (orange solid).

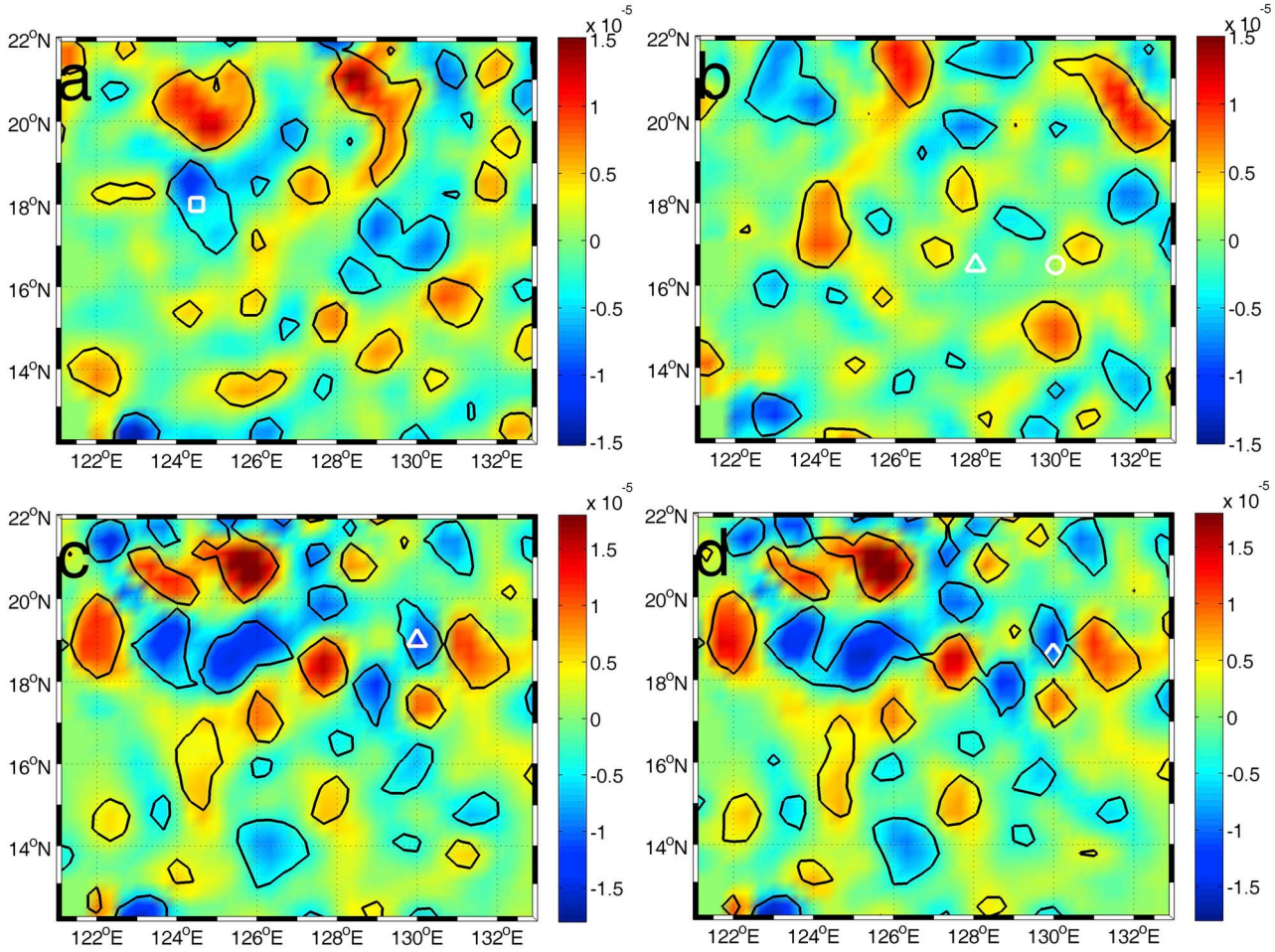

Figure 10. Geography of the geostrophic vorticity in s^{-1} computed from merged satellite sea surface height anomaly data at different time: (a) 12 December 2009 with the white square marking the location of the profile shown in Figure 6d, (b) 26 November 2010 with the white triangle and asterisk marking the locations of profiles shown in Figures 6a, 6b and 6c, (c) 22 July 1996 with the white triangle marking the location of profile shown in Figure 11a (orange solid), and (d) 24 July 1996 with the white diamond marking the location of profile shown in Figure 11a (red solid). Regions where the Okubo-Weiss parameter W less than -2×10^{-12} s^{-2} are indicated by thick black contours.

the lower bound of the internal wave band from the planetary value of the Coriolis frequency f to an effective Coriolis frequency $f_{eff} = f + (\zeta/2)$. Trapping will occur in the anticyclonic eddies where near inertial wave's intrinsic frequency can be less than the effective Coriolis frequency of the surrounding ocean, which leads to intense downward-propagating near inertial energy. Therefore the anticyclonic eddies are capable of strengthening the amount of energy propagating downward, and may be a potential factor accounting for the elevated mixing down to 900 m detected in the fourth profile.

[41] To verify our conjecture, we evaluated the geostrophic vorticity in terms of sea surface height anomaly as

$$\zeta = \frac{g}{f}\nabla^2\eta \tag{15}$$

where η is the merged satellite altimetry sea surface height anomaly (See Section Data and Methodology for detail), g the gravity acceleration, and ∇^2 the horizontal Laplacian operator. The eddies are identified based on the closed contours of the Okubo-Weiss parameter W, defined as the sum of the squares of the normal and shear components of strain minus the square of the geostrophic vorticity. This parameter is a measure of the relative importance of deformation and rotation, and is calculated based on surface height anomaly data [*Chelton et al.*, 2007]. Eddies, in which vorticity dominates strain, are marked by negative W. Here, closed contours of $W = -2 \times 10^{-12}$ s^{-2} were taken to define eddies following *Chelton et al.* [2007]. It can be seen from Figure 10a that the fourth profile was collected near the center of a strong anticyclonic eddy. As the downward-propagating near inertial energy under the anticyclonic eddy will also be horizontally trapped [*Kunze*, 1985], the energy-input region is probably located within the anticyclonic eddy. Because the eddy slowly moves westward with a velocity about 6 km d^{-1} and the most recent wind-energy

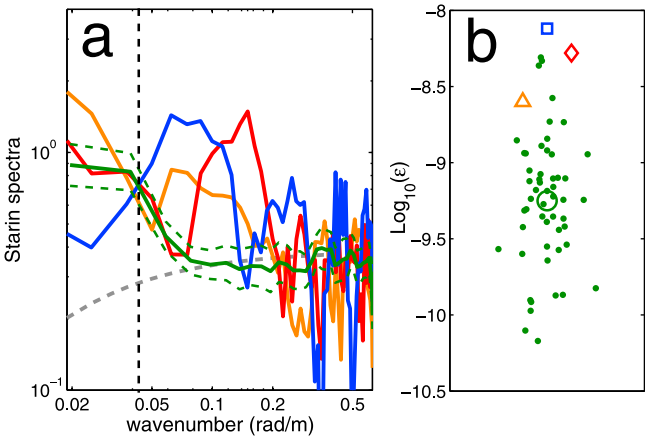

Figure 11. The diapycnal mixing in segment 600–900 m under strong anticyclonic eddies with the orange, red, and blue representing the profile collected on 22 July 1996, 24 July 1996 and 12 December 2009, respectively: (a) spectrum averaged among 53 profiles collected within 8°N–22°N, 124°E–130°E spanning from year 1993 to 2010 with no-eddy conditions (green solid line) and the 95% confidence interval based on a lognormal distribution (green dashed line). The gray dashed line is the GM model spectrum. (b) Scatterplot of dissipation rate of 53 profiles collected within 8°N–22°N, 124°E–130°E (green dots) and the mean value (green circle). The triangle, square, and diamond represent those collected under strong anticyclonic eddies.

burst is about a dozen of days ago, the energy-input region might be tens or hundreds of kilometers to the east of the station where the fourth profile was collected. On the contrary, the first three profiles were not located in any anticyclonic eddy when they were collected (Figure 10b). Therefore, it is likely that the elevated mixing down to 900 m detected in the fourth profile is probably due to the presence of anticyclonic eddies.

[42] To further verify the role of anticyclonic eddies in draining energy to great depth, we compare the dissipation rate in 600–900 m under strong anticyclonic eddies with that under none-eddy condition. In the region 8°N–22°N, 124°E–130°E, enhanced mixing over rough topography does not extend to the upper ocean. To amplify the sample size, all the profiles collected in this region are used here. There are 53 profiles collected spanning from year 1993 to 2010 under non-eddy conditions. (Note that a part of WOCE profiles were collected before year 1993. But they cannot be used here because the Satellite SSHA data began from 4 November 1992.) For each profile we evaluate the strain spectrum as well as the dissipation rate at segment 600–900 m (Figure 11). On the other hand, there are three distinctive profiles (including the one displayed in Figure 6d) located under strong anticyclonic eddies with the magnitude of central geostrophic vorticity larger than 10^{-5} s^{-1}. In addition to the profile shown in Figure 6d, the remaining two profiles were collected on 22 July 1996 and 24 July 1996, and locations are marked in Figures 10c and 10d with white triangle and diamond respectively. For these eddies, the horizontal gradient of geostrophic vorticity is about $O(10^{-10}$ m^{-1} $s^{-1})$, an order larger than the variation of the planetary value in the magnitude. So locally the effective Coriolis instead of the β-dispersion effect dominates the propagation of near inertial waves. At the segment 600–900 m, all these three profiles show elevated spectrum at lower wave numbers, i.e., between the lowest resolved wave number and 0.03 cpm (Figure 11a), and the values of dissipation rates are much higher than the mean value in the none-eddy condition (Figure 11b), further supporting the critical role of anticyclonic eddies in draining energy to great depth.

4. Validation of the Results

[43] As shown in section 2.2, the strain spectra are probably free from the contamination by background stratification and density noise between 300 m and 3000 m. However, in view of the uncertainties inherent in the fine-scale parameterization method with a fixed shear/strain variance ratio, a careful comparison between the estimates based on fine-scale parameterization method with those on Thorpe-scale method would be helpful to test the validity of our results. It should be noted that the Thorpe-scale method is not applicable to the WOCE data because of the limit of the vertical resolution (2 m). So we will apply this method only to the profiles collected during our recent hydrographic surveys. To get a stable estimate of the diffusivity from the overturn method, it has to be an average over a couple of profiles. Here we evaluate the geometric mean of diffusivity averaged among the profiles located over smooth bathymetry and at Luzon Strait respectively.

[44] Figures 12a and 12b show the mean ratio of diffusivity by fine-scale parameterization estimates to that by Thorpe-scale estimates over smooth topography and at Luzon Strait, respectively. Both methods give similar predictions

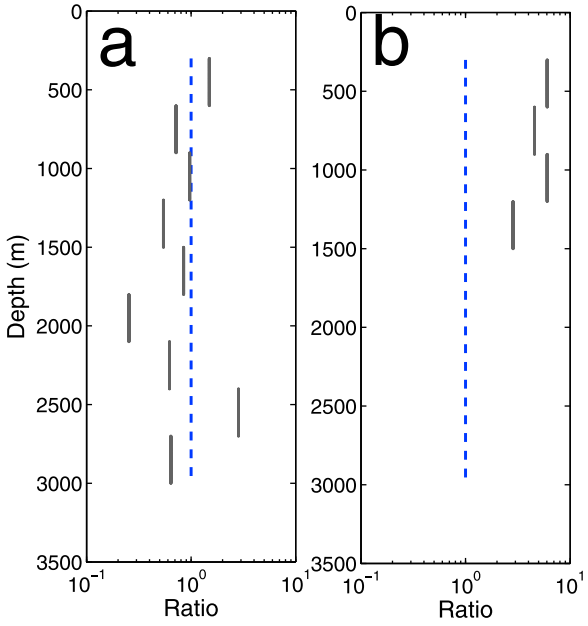

Figure 12. Ratio of diffusivity by fine-scale parameterization estimates to that by Thorpe-scale estimates based on (a) 19 profiles over smooth bathymetry and (b) 29 profiles at Luzon Strait. The deepest segment at Luzon Strait, i.e., 1500–1800 m is omitted since there is only one profile available.

for diapycnal diffusivity over smooth bathymetry. In the uppermost segment, estimate by a fine-scale parameterization method is about 1.5-fold of that by Thorpe-scale method, which might result from the fact that a 0.25-m vertical resolution is not sufficient to resolve most of the density overturns occurring in this region where the background stratification is relatively strong [*Galbraith and Kelley*, 1996]. Between 600 m and 1800 m, the estimates based on Thorpe-scale method is generally higher but the deviation is still within a factor of 2 (Figure 12a). In the deeper region, uncertainties become larger and the deviation reaches a factor of 4. Such larger deviation results from the reduced sample size. Actually, there are only three profiles available below 2000 m. (Note that although there are 19 profiles collected over smooth bathymetry during our four cruises, most have a maximal sampling depth less than 2000 m.) On the other hand, the deviation becomes larger at Luzon Strait with the estimates from the strain method higher than those from the Thorpe-scale method throughout the water column. As the mixing here is mainly furnished by both diurnal and semi-diurnal tidal dissipation, the shear/strain variance ratio might be overestimated by using a fixed value of 7, which might lead to an overestimation in strain method.

[45] It might be possible to deduce a guess of the value of the shear/strain variance ratio in the Luzon Strait by comparing our strain-based estimates with those relying on both shear and strain. *Tian et al.* [2009] estimated the diapycnal mixing in the Luzon Strait by using LADCP fine structure data. Their averaged diapycnal diffusivity in the upper 1000 m over Luzon Strait is 8.2×10^{-4} m^2 s^{-1}. As the value evaluated by *Tian et al.* [2009] is the arithmetic mean (Q. Yang, personal communication, 2011), we recalculate the arithmetic-mean diffusivity in the corresponding region using our profiles. Our estimate is about 3.1×10^{-3} m^2 s^{-1}, approximately 3.7-fold of that estimated by *Tian et al.* [2009]. Invoking the equation (3) gives a rough estimate for R_ω, i.e., 2.

[46] Considering that the methodologies used in our and their paper to evaluate strain variance are not completely the same with each other, and that the profiles used in these two studies are not located in the same places (note that while the diffusivity in Luzon Strait is generally about $O(10^{-3}$ m^2 s$^{-1})$, it also shows horizontal variability), it remains uncertain whether the deviation of our estimates from theirs is simply due to the different choices of R_ω. Therefore, we think that the deduced value for R_ω, i.e., 2 is a very rough estimate, and should be treated with caution. On the other hand, regardless of the exact value for R_ω, e.g., 2 or 7, the diffusivity at Luzon Strait is still at least an order of magnitude larger than that over smooth bathymetry, and the enhanced mixing here is thus reliable.

5. Summary and Discussion

[47] A fine-scale parameterization method is used to estimate both the spatial distribution and seasonal variation of diapycnal mixing in the subtropical northwestern Pacific. Several phenomena have been found as follows.

[48] 1. In the regions where the bathymetry is relatively smooth, the value of diffusivity away from the boundary is about O (10^{-5} m^2 s^{-1}), compatible to the values observed in the stratified midlatitude ocean interior.

[49] 2. Enhanced diapycnal mixing, i.e., O (10^{-4} m^2 s^{-1}) or larger has been found over rough topography such as the Central Basin Trough, Okidaito Ridge, the origin of the Kuroshio Current, and especially the Luzon Strait, which might result from dissipation of baroclinic energy generated when barotropic tides rub over rough topography.

[50] 3. The diapycnal mixing in the upper 600 m is stirred by the wind work on near inertial motions with most wind-input energy dissipated within this region. Such a wind-furnished mixing is further revealed by distinct seasonal variation of diapycnal diffusivity found in the uppermost segment with strong (weak) mixing corresponding to strong (weak) wind work in winter (summer).

[51] 4. Enhanced downward-propagating energy, i.e., extending to 1000-m depth has been found in the presence of anticyclonic eddies, pointing to the important role of anticyclonic eddies in draining energy to great depth and thus maintaining the subsurface and deep ocean mixing.

[52] It has been argued whether a substantial portion of energy flux from the wind to mixed layer near inertial motions can propagate downward to great depth and support the subsurface and deep ocean mixing [*Wunsch and Ferrari*, 2004]. So far both modeling and observational studies have not reached consensus [*Danioux et al.*, 2008; *Jing and Wu*, 2010; *Kunze et al.*, 2006; *Zhai et al.*, 2005, 2009]. Based on historically accumulated profiles along 137°E, *Jing and Wu* [2010] found that the seasonality of diapycnal mixing in the region south of Japan Island penetrates to more than 1500-m depth, which points to the important role of wind work on near inertial motions in maintaining the subsurface and deep-ocean mixing. However, in the subtropical northwestern Pacific, we find that the seasonality of mixing is only confined to the upper 600 m. Most of the wind-input energy is probably dissipated in the upper 600 m and is not able to further propagate downward to supply energy for mixing in deeper region. The two studies appear to contradict each other. However, as shown in this paper, the anticyclonic eddies play an important role in draining energy to great depth. So the contradiction here might probably be due to much stronger eddy variability to the south of Japan Island than that in the subtropical northwestern Pacific. If this conjecture can hold, the wind-input near inertial energy might have an important role in sustaining the subsurface and deep ocean mixing, as regions of strong near-inertial energy input from wind to the ocean are also regions of strong mesoscale variability. This may help fill up the gap between the energy needed to maintain abyssal stratification and tidal dissipation in the open ocean [*Wunsch and Ferrari*, 2004].

[53] **Acknowledgments.** This work is supported by China National Key Basic Research Project (2007CB411800), China National Natural Science Foundation (NSFC) Distinguished Young Investigator Project (40788002), and NSFC Innovation Team project (40921004). We thank National Oceanographic Data Center for providing WOCE data through the open access (http://cchdo.ucsd.edu/pacific.html) and AVISO for providing the Ssalto/Duacs products.

References

Alford, M. H. (2003), Improved global maps and 54-year history of wind-work on ocean inertial motions, *Geophys. Res. Lett.*, *30*(8), 1424, doi:10.1029/2002GL016614.

Alford, M. H., and M. C. Gregg (2001), Near-inertial mixing: Modulation of shear, strain and microstructure at low latitude, *J. Geophys. Res.*, *106*, 16,947–16,968, doi:10.1029/2000JC000370.

Alford, M. H., and M. Whitmont (2007), Seasonal and spatial variability of near-inertial kinetic energy from historical moored velocity records, *J. Phys. Oceanogr.*, *37*, 2022–2037, doi:10.1175/JPO3106.1.

Althaus, A. M., E. Kunze, and T. B. Sanford (2003), Internal tide radiation from Mendocino Escarpment, *J. Phys. Oceanogr.*, *33*, 1510–1527, doi:10.1175/1520-0485(2003)033<1510:ITRFME>2.0.CO;2.

Carter, G. S., and M. C. Gregg (2002), Intense variable mixing near the head of Monterey Submarine Canyon, *J. Phys. Oceanogr.*, *32*, 3145–3165, doi:10.1175/1520-0485(2002)032<3145:IVMNTH>2.0.CO;2.

Chelton, D. B., M. G. Schlax, R. M. Samelson, and R. A. de Szoeke (2007), Global observations of large oceanic eddies, *Geophys. Res. Lett.*, *34*, L15606, doi:10.1029/2007GL030812.

D'Asaro, E. A. (1985), The energy flux from the wind to near inertial motions in the mixed-layer, *J. Phys. Oceanogr.*, *15*, 1043–1059, doi:10.1175/1520-0485(1985)015<1043:TEFFTW>2.0.CO;2.

Danioux, E., P. Klein, and P. Rivière (2008), Propagation of wind energy into the deep ocean through a fully turbulent mesoscale eddy field, *J. Phys. Oceanogr.*, *38*, 2224–2241, doi:10.1175/2008JPO3821.1.

Dillon, T. M. (1982), Vertical overturns: A comparison of Thorpe and Ozmidov length scales, *J. Geophys. Res.*, *87*, 9601–9613, doi:10.1029/JC087iC12p09601.

Dillon, T. M. (1984), The energetics of overturning structures: Implications for the theory of fossil turbulence, *J. Phys. Oceanogr.*, *14*, 541–549, doi:10.1175/1520-0485(1984)014<0541:TEOOSI>2.0.CO;2.

Egbert, G. D., and R. D. Ray (2000), Significant dissipation of tidal energy in the deep ocean inferred from satellite altimeter data, *Nature*, *405*, 775–778, doi:10.1038/35015531.

Ferron, B., H. Mercier, K. Speer, A. Gargett, and K. Polzin (1998), Mixing in the Romanche Fracture Zone, *J. Phys. Oceanogr.*, *28*, 1929–1945, doi:10.1175/1520-0485(1998)028<1929:MITRFZ>2.0.CO;2.

Finnigan, T., D. Luther, and R. Lukas (2002), Observations of enhanced diapycnal mixing near the Hawaiian Ridge, *J. Phys. Oceanogr.*, *32*, 2988–3002, doi:10.1175/1520-0485(2002)032<2988:OOEDMN>2.0.CO;2.

Galbraith, P. S., and D. E. Kelley (1996), Identifying overturns in CTD profiles, *J. Atmos. Oceanic Technol.*, *13*, 688–702, doi:10.1175/1520-0426(1996)013<0688:IOICP>2.0.CO;2.

Gargett, A., and T. Garner (2008), Determining Thorpe scales from ship-lowered CTD density profiles, *J. Atmos. Oceanic Technol.*, *25*, 1657–1670, doi:10.1175/2008JTECHO541.1.

Garrett, C. (2001), What is the "near-inertial" band and why is it different from the rest of the internal wave spectrum?, *J. Phys. Oceanogr.*, *31*, 962–971, doi:10.1175/1520-0485(2001)031<0962:WITNIB>2.0.CO;2.

Gregg, M. C. (1987), Diapycnal mixing in the thermocline: A review, *J. Geophys. Res.*, *92*, 5249–5286, doi:10.1029/JC092iC05p05249.

Gregg, M. C., and E. Kunze (1991), Internal wave shear and strain in Santa Monica Basin, *J. Geophys. Res.*, *96*, 16,709–16,719, doi:10.1029/91JC01385.

Jing, Z., and L. Wu (2010), Seasonal variation of turbulent diapycnal mixing in the northwestern Pacific stirred by wind stress, *Geophys. Res. Lett.*, *37*, L23604, doi:10.1029/2010GL045418.

Kalnay, E., et al. (1996), The NCEP/NCAR 40-year reanalysis project, *Bull. Am. Meteorol. Soc.*, *77*, 437–471, doi:10.1175/1520-0477(1996)077<0437:TNYRP>2.0.CO;2.

Klymak, J. M., et al. (2006), An estimate of tidal energy lost to turbulence at the Hawaiian Ridge, *J. Phys. Oceanogr.*, *36*, 1148–1164, doi:10.1175/JPO2885.1.

Kunze, E. (1985), Near-inertial propagation in geostrophic shear, *J. Phys. Oceanogr.*, *15*, 544–565, doi:10.1175/1520-0485(1985)015<0544:NIWPIG>2.0.CO;2.

Kunze, E., and J. M. Toole (1997), Tidally driven vorticity, diurnal shear, and turbulence atop Fieberling Seamount, *J. Phys. Oceanogr.*, *27*, 2663–2693, doi:10.1175/1520-0485(1997)027<2663:TDVDSA>2.0.CO;2.

Kunze, E., E. Firing, J. M. Hummon, T. K. Chereskin, and A. M. Thurnherr (2006), Global abyssal mixing inferred from lowered ADCP shear and CTD strain profiles, *J. Phys. Oceanogr.*, *36*, 1553–1576, doi:10.1175/JPO2926.1.

Lilliefors, H. (1967), On the Kolmogorov–Smirnov test for normality with mean and variance unknown, *J. Am. Stat. Assoc.*, *62*, 399–402, doi:10.2307/2283970.

Lueck, R. G., and T. D. Mudge (1997), Topographically induced mixing around a shallow seamount, *Science*, *276*, 1831–1833, doi:10.1126/science.276.5320.1831.

Munk, W. H. (1966), Abyssal recipes, *Deep-Sea Res.*, *13*, 207–230.

Naveira Garabato, A. C., D. P. Stevens, and K. J. Heywood (2003), Water-mass conversion, fluxes and mixing in the Scotia Sea diagnosed by an inverse model, *J. Phys. Oceanogr.*, *33*, 2565–2587, doi:10.1175/1520-0485(2003)033<2565:WMCFAM>2.0.CO;2.

Osborn, T. R. (1980), Estimates of the local rate of vertical diffusion from dissipation measurements, *J. Phys. Oceanogr.*, *10*, 83–89, doi:10.1175/1520-0485(1980)010<0083:EOTLRO>2.0.CO;2.

Pollard, R. T., and R. C. Millard (1970), Comparison between observed and simulated wind-generated inertial oscillations, *Deep Sea Res. Oceanogr. Abstr.*, *17*, 813–821, doi:10.1016/0011-7471(70)90043-4.

Polzin, K. L. (1996), Statistics of the Richardson number: Mixing models and finestructure, *J. Phys. Oceanogr.*, *26*, 1409–1425, doi:10.1175/1520-0485(1996)026<1409:SOTRNM>2.0.CO;2.

Polzin, K. (1999), A rough recipe for the energy balance of quasi-steady internal Lee waves, in *Internal Wave Modelling*, edited by D. Muller and D. Henderson, pp. 117–128, Univ. of Hawai'i at Monoa, Honolulu.

Polzin, K. (2004), Idealized solutions for the energy balance of finescale internal wave field, *J. Phys. Oceanogr.*, *34*, 231–246, doi:10.1175/1520-0485(2004)034<0231:ISFTEB>2.0.CO;2.

Polzin, K. L., J. M. Toole, and R. W. Schmitt (1995), Finescale parameterizations of turbulent mixing, *J. Phys. Oceanogr.*, *25*, 306–328, doi:10.1175/1520-0485(1995)025<0306:FPOTD>2.0.CO;2.

Polzin, K. L., J. M. Toole, J. R. Ledwell, and R. W. Schmitt (1997), Spatial variability of turbulent mixing in the abyssal ocean, *Science*, *276*, 93–96, doi:10.1126/science.276.5309.93.

Polzin, K. L., E. Kunze, J. Hummon, and E. Firing (2002), The finescale response of lowered ADCP velocity profiles, *J. Atmos. Oceanic Technol.*, *19*, 205–224, doi:10.1175/1520-0426(2002)019<0205:TFROLA>2.0.CO;2.

Richards, K. J., S.-P. Xie, and T. Miyama (2009), Vertical mixing in the ocean and its impact on the coupled ocean-atmosphere system in the eastern tropical Pacific, *J. Clim.*, *22*(13), 3703–3719, doi:10.1175/2009JCLI2702.1.

Roemmich, D., S. Hautala, and D. Rudnick (1996), Northward abyssal transport through the Samoan Passage and adjacent regions, *J. Geophys. Res.*, *101*, 14,039–14,055, doi:10.1029/96JC00797.

Saenko, O., and W. Merryfield (2005), On the effect of topographically enhanced mixing on the global ocean circulation, *J. Phys. Oceanogr.*, *35*, 826–834, doi:10.1175/JPO2722.1.

St. Laurent, L., and C. Garrett (2002), The role of internal tides in mixing the deep ocean, *J. Phys. Oceanogr.*, *32*, 2882–2899, doi:10.1175/1520-0485(2002)032<2882:TROITI>2.0.CO;2.

St. Laurent, L. C., J. M. Toole, and R. W. Schmitt (2001), Buoyancy forcing by turbulence above rough topography in the abyssal basin, *J. Phys. Oceanogr.*, *31*, 3476–3495, doi:10.1175/1520-0485(2001)031<3476:BFBTAR>2.0.CO;2.

St. Laurent, L. C., H. L. Simmons, and S. R. Jayne (2002), Estimating tidally driven mixing in the deep ocean, *Geophys. Res. Lett.*, *29*(23), 2106, doi:10.1029/2002GL015633.

Thorpe, S. (1977), Turbulence and mixing in a Scottish Loch, *Philos. Trans. R. Soc. London, Ser. A*, *286*, 125–181, doi:10.1098/rsta.1977.0112.

Tian, J., Q. Yang, and W. Zhao (2009), Enhanced diapycnal mixing in the South China Sea, *J. Phys. Oceanogr.*, *39*, 3191–3203, doi:10.1175/2009JPO3899.1.

Toggweiler, J., and B. Samuels (1998), On the ocean's large-scale circulation near the limit of no vertical mixing, *J. Phys. Oceanogr.*, *28*, 1832–1852, doi:10.1175/1520-0485(1998)028<1832:OTOSLS>2.0.CO;2.

Wunsch, C., and R. Ferrari (2004), Vertical mixing, energy and the general circulation of the oceans, *Annu. Rev. Fluid Mech.*, *36*, 281–314, doi:10.1146/annurev.fluid.36.050802.122121.

Zhai, X., R. J. Greatbatch, and J. Zhao (2005), Enhanced vertical propagation of storm-induced near-inertial energy in an eddying ocean channel model, *Geophys. Res. Lett.*, *32*, L18602, doi:10.1029/2005GL023643.

Zhai, X., R. J. Greatbatch, C. Eden, and T. Hibiya (2009), On the loss of wind-induced near-inertial energy to turbulent mixing in the upper ocean, *J. Phys. Oceanogr.*, *39*, 3040–3045, doi:10.1175/2009JPO4259.1.

Z. Chen, Z. Jing, L. Li, X. Liang, C. Liu, Q. Liu, and L. Wu, Physical Oceanography Laboratory, Ocean University of China, 238 Songling Rd., Qingdao 266100, China. (jingzhao198763@sina.com)

D. Hu, Key Laboratory of Ocean Circulation and Wave, Chinese Academy of Sciences, 7 Nanhai Rd., Qingdao 266071, China.